Smart Structures and Systems, *Vol. 20, No. 2 (2017) 181-195*
DOI: https://doi.org/10.12989/sss.2017.20.2.181

Quantitative damage identification in tendon anchorage via PZT interface-based impedance monitoring technique

Thanh-Canh Huynh[a] and Jeong-Tae Kim[*]

Department of Ocean Engineering, Pukyong National University,
45 Yongso-ro, Daeyeon 3-dong, Nam-Gu, Busan 608-737, Republic of Korea

(Received January 8, 2017, Revised March 30, 2017, Accepted April 8, 2017)

Abstract. In this study, the severity of damage in tendon anchorage caused by the loss of tendon forces is quantitatively identified by using the PZT interface-based impedance monitoring technique. Firstly, a 2-DOF impedance model is newly designed to represent coupled dynamic responses of PZT interface-host structure. Secondly, the 2-DOF impedance model is adopted for the tendon anchorage system. A prototype of PZT interface is designed for the impedance monitoring. Then impedance signatures are experimentally measured from a laboratory-scale tendon anchorage structure with various tendon forces. Finally, damage severities of the tendon anchorage induced by the variation of tendon forces are quantitatively identified from the phase-by-phase model updating process, from which the change in impedance signatures is correlated to the change in structural properties.

Keywords: damage identification; tendon anchorage; PZT interface; impedance monitoring; tendon force; 2-DOF impedance model

1. Introduction

Over the past decades, many researchers have studied damage detection in structural systems by monitoring the global responses (Stubbs and Osegueda 1990, Doebling *et al.* 1998, Huynh *et al.* 2013, Kim *et al.* 2014) and the local responses (Liang *et al.* 1994, Park *et al.* 2001, Kim *et al.* 2006, Ni *et al.* 2010 and 2012, Li *et al.* 2014, Huynh and Kim 2017). Among various local dynamic responses, the electromechanical impedance has been found as a promising dynamic feature to detect the local damage for various types of structures. Recently, the electromechanical impedance-based method has been implemented for structural health monitoring of tendon anchorage systems (Kim *et al.* 2010, Nguyen and Kim 2012, Huynh and Kim 2014, Park *et al.* 2015, Huynh *et al.* 2015a). Nguyen and Kim (2012) developed a PZT interface device that enables wireless impedance monitoring by setting the frequency band as low as less than 100 kHz. Huynh and Kim (2014) developed a surface-mountable PZT interface technique that could monitor the change in impedance signatures caused by the change in tendon forces in the anchorage system. Despite those research efforts, there still exists a need to justify the feasibility of the PZT interface-based impedance monitoring by verifying the relationship between the anchor force and the structural response of the PZT interface.

As the impedance monitoring technique has been successfully implemented on various types of structures, the quantitative damage detection by the impedance-based technique has become an important issue for complex structural connections. Since the impedance technique is not based on any particular physical models, it is very difficult to quantitatively correlate the change in impedance signatures to the change in structural properties. As the result, the technique provides limited information on the nature of damage. Up-to-date, most of experimental studies used the impedance technique for qualitative health monitoring (Chaudhry *et al.* 1995, Ayres *et al.* 1998, Soh *et al.* 2000, Park *et al.* 2001, Koh *et al.* 2003, Park *et al.* 2005, Giurgiutiu and Zagrai 2005, Kim *et al.* 2010, Min *et al.* 2010, Huynh *et al.* 2016a). In most applications, the impedance signatures have been qualitatively classified for the alert of damage occurrence due to the target structure's complexity and the difficulty in high-frequency modelling.

So far, there has been a few researches reported on the quantitative health monitoring in structural connections using the impedance signatures. Ritdumrongkul *et al.* (2004) employed the spectral element method to model the PZT-bolted joint system and applied a mathematical minimization method to quantitatively estimate the structural parameters of the joint. However, the frequency band considered in their study was relatively low, less than 2.5 kHz, as compared to the effective frequency bands commonly used in the real implementation of the impedance technique. Lopes *et al.* (2000) and Min *et al.* (2012) proposed the impedance-based technique combining with the artificial neural network (ANN) technique to identify damage types and severities in structural connections. As with the ANN-based technique, a large amount of the impedance measurements should be conducted on the host structure under both intact and

*Corresponding author, Ph.D. Professor
E-mail: idis@pknu.ac.kr
[a] Post-Doctoral Researcher
E-mail: ce.huynh@gmail.com

ISSN: 1738-1584 (Print), 1738-1991 (Online)

damage states. The challenging job of their studies is to feed the ANN by acquiring suitable impedance data-sets of training scenarios from existing structures; otherwise, the structures should be accurately modelled to train the ANN by high-frequency impedance simulations.

In this study, the severity of damage in tendon anchorage caused by the loss of tendon forces is quantitatively identified by using the PZT interface-based impedance monitoring technique. The following approaches are implemented. Firstly, a 2-DOF impedance model is newly designed to represent coupled dynamic responses of PZT interface-host structure. Secondly, the PZT interface-based monitoring of tendon anchorage system is described. The 2-DOF impedance model is adopted for the tendon anchorage system. A prototype of PZT interface is designed for the impedance monitoring. Then impedance signatures are experimentally measured from a laboratory-scale tendon anchorage structure with various tendon forces. Finally, damage severities of the tendon anchorage induced by the variation of tendon forces are quantitatively identified. A finite element (FE) model of the PZT interface-anchorage system is simulated. A phase-by-phase model updating process is proposed to fine-tune the FE model of the tendon anchorage. Then the model updating is performed to correlate the change in impedance signatures to the change in structural properties, both of which are induced by the variation of tendon forces.

2. Electromechanical impedance model of PZT interface-host structure

2.1 Theory of electromechanical impedance

Piezoelectric materials have been widely adopted as promising smart materials for SHM applications due to their unique properties (Park *et al.* 2003). Their considerable advantages include low-cost price, lightweight material, robustness and multiforms ranging from thin patches to complex shapes (Giurgiutiu 2014). By utilising the inverse effect, Liang *et al.* (1996) proposed the concept of electromechanical (EM) impedance for PZT actuator-driven mechanical systems which is based on the coupling of mechanical and electrical characteristics.

To acquire the EM impedance signatures from the monitored structure, a piezoelectric material (e.g., PZT) is surface-bonded to the structure, as shown in Fig. 1(a). Liang *et al.* (1996) proposed a 1-DOF impedance model of the PZT-structure system to explain the interaction between the PZT and the host structure, as shown in Fig. 1(b). Under an input harmonic voltage $V(\omega)$, a piezoelectric deformation of PZT is induced due to the inverse piezoelectric effect. This piezoelectric deformation simultaneously induces a force $F(\omega)$ into the host structure and the PZT (see Fig. 1(a)). For the 1-DOF system shown in Fig. 1(b), the structural mechanical (SM) impedance of the host structure $Z_s(\omega)$ is obtained by the ratio of the force $F(\omega)$ to the velocity $\dot{u}(\omega)$ at the PZT driving point (Liang *et al.* 1996), as follows

$$Z_s(\omega) = \frac{F(\omega)}{\dot{u}(\omega)} = c + m\frac{\omega^2 - \omega_n^2}{\omega} i \tag{1}$$

in which c and m signify the damping coefficient and the mass of the host structure, respectively; ω_n represents the angular natural frequency of the host structure; and ω is the angular frequency of the excitation voltage. From Eq. (1), the SM impedance of the host structure is a function of the mass, damping, and stiffness (m, c, k). This means any change in the structural parameters of the host structure would lead to the change in the SM impedance.

In practice, the electric current $I(\omega)$ is measured and then it is utilized to calculate the EM impedance, $Z(\omega)$, as follows (Liang *et al.* 1996)

$$Z(\omega) = \frac{V}{I} = \left\{ i\omega \frac{w_a l_a}{t_a} \left[\hat{\varepsilon}_{33}^T - \frac{1}{Z_a(\omega)/Z_s(\omega)+1} d_{31}^2 \hat{Y}_{11}^E \right] \right\}^{-1} \tag{2}$$

where $\hat{Y}_{11}^E = (1+i\eta)Y_{11}^E$ is the complex Young's modulus of the PZT patch at zero electric field; $\hat{\varepsilon}_{33}^T = (1-i\delta)\varepsilon_{33}^T$ is the complex dielectric constant at zero stress; d_{31} is the piezoelectric coupling constant in *1*-direction at zero stress; and w_a, l_a, and t_a are the width, length, and thickness of the piezoelectric transducer, respectively. The parameters η and δ are structural damping loss factor and dielectric loss factor of piezoelectric material, respectively.

From Eq. (2), the EM impedance, $Z(\omega)$, contains both the SM impedance of the host structure, $Z_s(\omega)$, and that of the PZT sensor, $Z_a(\omega)$. Therefore, any change in the structural parameters (k, m, c) of the host structure can be represented by the change in the EM impedance obtained from the PZT sensor. From previous studies (Sun *et al.* 1995, Park *et al.* 2006), it is shown that the real part of EM impedance contains much more information of structural integrity than the imaginary part.

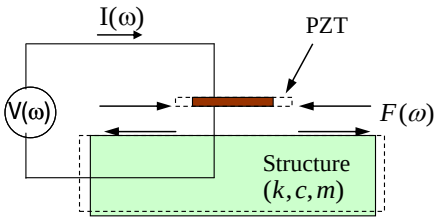

(a) Coupling interaction

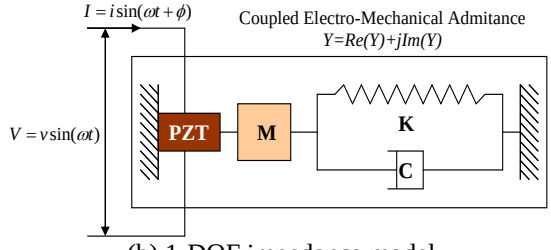

(b) 1-DOF impedance model

Fig. 1 Electromechanical interaction between PZT and host structure

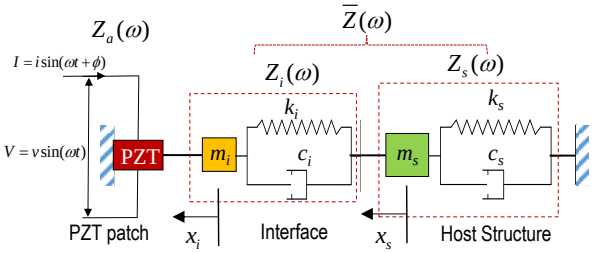

Fig. 2 2-DOF impedance model of PZT interface-host structure system

Therefore, the real part is often used for the impedance-based damage detection while the imaginary part is useful for monitoring the health status and bonding condition of the PZT sensor. However, an issue of the 1-DOF impedance model is on setting the sensitive frequency band of impedance signatures which is governed by the target structure's parameters, as described in Eq. (2). For most cases, the sensitive frequency band is unknown and traditionally determined by try-and-error.

2.2 2-DOF impedance model of PZT interface-host structure

On the basis of the previous studies (Liang *et al.* 1996, Xu and Liu 2002, Park *et al.* 2009), an EM impedance model is designed to represent coupled dynamic responses of PZT interface-host structure, as shown in Fig. 2. The PZT interface-host structure is still modelled as a spring-mass-damper (SMD) system. In this 2-DOF system, one refers to the host structure represented by the impedance Z_s and the other refers to the interface represented by its impedance Z_i.

For the 2-DOF system shown in Fig. 2, the equation of motion under an external force F_i at the PZT driving point can be written as

$$\begin{bmatrix} m_i & 0 \\ 0 & m_s \end{bmatrix}\begin{Bmatrix} \ddot{x}_i \\ \ddot{x}_s \end{Bmatrix} + \begin{bmatrix} c_i & -c_i \\ -c_i & c_i + c_s \end{bmatrix}\begin{Bmatrix} \dot{x}_i \\ \dot{x}_s \end{Bmatrix} + \begin{bmatrix} k_i & -k_i \\ -k_i & k_i + k_s \end{bmatrix}\begin{Bmatrix} x_i \\ x_s \end{Bmatrix} = \begin{Bmatrix} F_i \\ 0 \end{Bmatrix} \tag{3}$$

where m_i, c_i, k_i and m_s, c_s, k_s are the masses, damping coefficients, and spring stiffness of the interface and the host structure generated by the PZT driving point, respectively; $x_i, \dot{x}_i, \ddot{x}_i$ and $x_s, \dot{x}_s, \ddot{x}_s$ are the displacements, velocities, and accelerations which correspond to the masses m_i and m_s, respectively. If the external force is harmonic as

$$F_i = F_{io} e^{i\omega t} \tag{4}$$

where ω is the forcing frequency and F_{io} is the forcing magnitude. The steady state solution can be written as

$$x_j = X_j e^{i\omega t}; \qquad j = i, s \tag{5}$$

where X_i and X_s are, in general, complex quantities that depend on ω and system parameters. By substituting Eqs. (4) and (5) into Eq. (3), we can obtain

$$\begin{bmatrix} -\omega^2 m_i + i\omega c_i + k_i & -i\omega c_i - k_i \\ -i\omega c_i - k_i & -\omega^2 m_s + i\omega(c_i + c_s) + (k_i + k_s) \end{bmatrix}\begin{Bmatrix} X_i \\ X_s \end{Bmatrix} = \begin{Bmatrix} F_{io} \\ 0 \end{Bmatrix} \tag{6}$$

Or

$$\begin{bmatrix} K_{11} & K_{12} \\ K_{12} & K_{22} \end{bmatrix}\begin{Bmatrix} X_i \\ X_s \end{Bmatrix} = \begin{Bmatrix} F_{io} \\ 0 \end{Bmatrix} \tag{7}$$

where the terms $[K_{ij}]$, i,j = 1, 2 are the dynamic stiffness (Xu and Liu 2002). The solutions of Eq. (7) can be obtained by inversing the dynamic stiffness matrix, as follows

$$X_i = \frac{K_{22}(\omega)F_{io}}{K_{11}(\omega)K_{22}(\omega) - K_{12}^2(\omega)}; \quad X_s = \frac{-K_{12}(\omega)F_{io}}{K_{11}(\omega)K_{22}(\omega) - K_{12}^2(\omega)} \tag{8}$$

where X_i and X_s are displacement quantities of the two coupled vibration modes for the interface-host structure system. By substituting Eq. (8) into Eq. (5) and taking derivative, the velocity of the interface at the PZT driving point can be obtained as

$$\dot{x}_i = i\omega X_1 e^{i\omega t} = \frac{i\omega K_{22}(F_{io}e^{i\omega t})}{K_{11}K_{22} - (K_{12})^2} = \frac{i\omega K_{22}F_i}{K_{11}K_{22} - (K_{12})^2} \tag{9}$$

The SM impedance $\bar{Z}(\omega)$ of the interface-host structure system at the PZT driving point is defined as the ratio between the excitation force F_i and the velocity $\dot{x}$ as

$$\bar{Z}(\omega) = \frac{F_i}{\dot{x}_i} = \frac{K_{11}K_{22} - (K_{12})^2}{i\omega K_{22}} \tag{10}$$

By substituting Eq. (10) into Eq. (2), the EM impedance response of the 2-DOF model of the PZT interface-host structure system can be obtained as

$$Z(\omega) = \left\{ i\omega \frac{w_a l_a}{t_a}\left[\hat{\varepsilon}_{33}^T - \frac{1}{Z_a(\omega)/\bar{Z}(\omega) + 1} d_{31}^2 \hat{Y}_{11}^E \right] \right\}^{-1} \tag{11}$$

where the electrical impedance $Z_a(\omega)$ of the PZT patch (width w_a, length l_a and thickness t_a) can be computed based on previous works (Liang *et al.* 1996, Xu and Liu 2002, Bhalla and Soh 2004) as

$$Z_a(\omega) = -i\frac{\hat{Y}_{11}^E w_a t_a}{\omega l_a} \tag{12}$$

From the above equations, it is noted that the present 2-DOF impedance model contains two resonant peaks in its impedance signatures which represent the two coupled vibration modes out of the PZT interface-host structure system. That is the unique difference of the proposed model from the previous models by Liang *et al.* (1996), Xu and

Table 1 Material properties and geometric sizes of the PZT patch (Park *et al.* 2009)

Y^E_{11} (N/m^2)	ρ (kg/m^3)	d_{31} (m/V)	ε^T_{33} ($Farads/m$)	δ	η	w_a (mm)	t_a (mm)	l_a (mm)
$6.3\text{x}10^{10}$	7650	$-1.66\ \text{x}10^{-10}$	$1.5\text{x}10^{-8}$	0.005	0.001	25.4	0.254	25.4

Liu (2002), and Park *et al.* (2008). Since the 2-DOF impedance model represents the structural parameters of both the interface device and the host structure, any structural change occurred in the host structure (or the PZT interface) can result in the change in the measured EM impedance signatures. Therefore, the structural integrity of the host structure can be estimated by monitoring these impedance changes. According to Eq. (11), the sensitive frequency band of impedance signatures can be predetermined by controlling the coupled SM impedance $\bar{Z}$ of the interface-host structure. Therefore, the issue of setting the sensitive frequency band in impedance monitoring practices can be solved by using the 2-DOF impedance model.

2.3 Numerical verification of 2-DOF impedance model

To demonstrate the feasibility of the proposed EM impedance model for damage detection, a simple example of the 2-DOF SMD model of the PZT interface-host structure system is investigated. The material properties and geometric sizes of the PZT patch are listed in Table 1 (Park *et al.* 2009). The SMD of the host structure is set as follows: m_s = 1 (kg), c_s = 125 ($N/m.s^{-1}$), and k_s = $5\text{x}10^{10}$ (N/m) while that of the interface is selected as: m_i = 0.2 (kg), c_i = 125 ($N/m.s^{-1}$), and k_i = $1\text{x}10^{10}$ (N/m).

The structural changes in the host structure are simulated by sequentially reducing its spring stiffness k_s up to 10 %, 20 %, and 30 %. Fig. 3 shows the impedance signatures of the EM model under various stiffness reductions in the host structure. As observed in the figure, there exist two impedance peaks corresponding to the two vibration modes of the 2-DOF impedance model. The first impedance peak has relatively higher magnitude than the second one. It is found that the change in the host structure's stiffness causes the decrease in the resonant frequencies. Note that the impedance peaks represent the significant contributions of the SM impedance to the EM impedance (Huynh and Kim 2014).

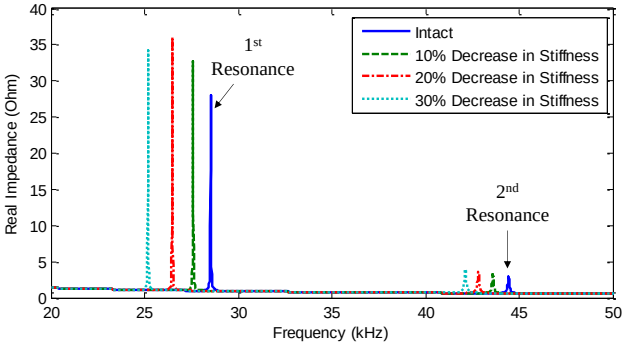

Fig. 3 Impedance variations under stiffness changes in host structure

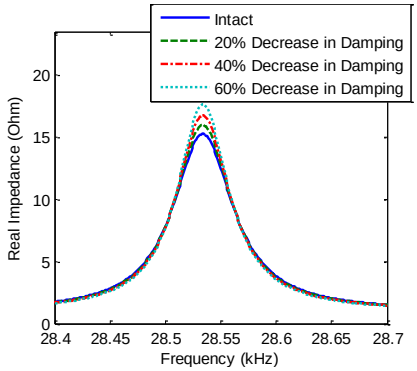

(a) First resonance

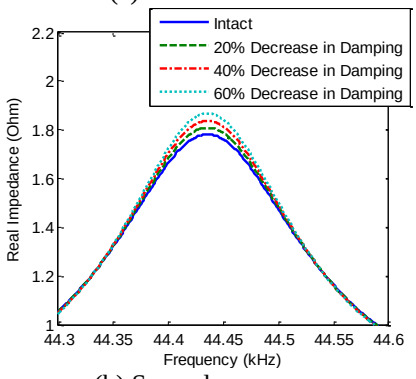

(b) Second resonance

Fig. 4 Impedance variations under damping changes in host structure

The effect of the damping variation in the host structure is also examined by sequentially reducing the damping coefficient c_s up to 20%, 40%, and 60%. Fig. 4 shows the EM impedance signatures of the first and second resonances under various damping changes in the host structure.

It is found that the damping reduction causes the slight increase in the peaks' magnitudes while the resonant frequencies remain unchanged. The increased magnitude of the resonant peaks due to the damping reduction is well-agreed with the previous study by Park *et al.* (2008). Conclusively, it has been proved that the change in the structural parameters of the host structure can be indirectly detected by the change in the EM impedance obtained from the PZT interface.

3. PZT interface-based impedance monitoring of tendon anchorage system

3.1 2-DOF impedance model of PZT interface-anchorage system

Under the prestress force, a system of the tendon anchorage can be modelled by connection components (i.e.,

bearing plate, anchor block, tendon) and contact forces, as shown in Fig. 5(a). The prestress force is modelled by a tendon force acting on the anchor block, and transformed to the contact pressure and bearing stress in the interfaces of the anchor block and bearing plate.

The interaction mechanism of the contact interfaces can be simplified by the two-dimensional damping and spring stiffness in normal and transverse directions, as shown in Fig. 5(b). According to the contact mechanism (Johnson 1985), the interfacial spring stiffness and damping values represent the amount of contact pressure and stress field acting on the interface. From the fact that the variation of interfacial stiffness and damping parameters are associated with the variation of contact pressure (Ritdumrongkul *et al.* 2004), the variation of tendon force can be treated as the variation of those structural parameters at the contact interface.

As also shown in Fig. 5(b), the PZT interface is mounted on the bearing plate to monitor the variation of structural parameters of the tendon anchorage, which can be induced by the loss of prestressing force. As tightly bonded to the surface of the bearing plate, the stress fields of the PZT interface become almost equivalent to those of the bearing plate on its surface, while the top and bottom mid-surfaces are freely deformed along with the deformation of the bearing plate. Therefore, any changes in the structural parameters of the bearing plate (e.g., contact stiffness), would lead to the change in the EM impedance response of the PZT interface.

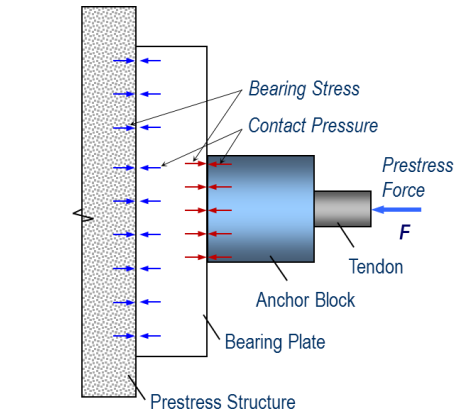

(a) Force equilibrium state

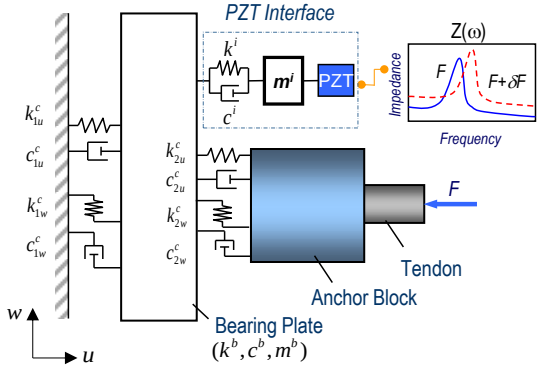

(b) 2-DOF impedance model

Fig. 5 Structural model of tendon anchorage system (Huynh and Kim 2014)

3.2 Design of PZT interface for tendon anchorage

3.2.1 Prototype design of PZT interface

Based on the proposed 2-DOF impedance model, the dynamic characteristics of the PZT interface-host structure system is closely associated with the resonant peaks of the impedance signatures (i.e., effective frequency ranges). Therefore, the effective frequency ranges for the impedance-based monitoring can be predetermined by controlling the structural parameters of the PZT interface.

As shown in Fig. 6, the mountable PZT interface device is conceptually designed on the basis of the 2-DOF impedance model. The prototype of the interface device is a beam-like structure with a PZT sensor at the middle, see Fig. 6(a). The interface structure has a flexible beam section in the middle and the fixed-fixed boundary by two outside contact surfaces. The flexible section, where the PZT sensor is installed, is intentionally designed to allow flexural vibration responses of the interface according to piezoelectric deformations of the PZT sensor.

Among various piezoelectric sensors, PZT, PVDF and MFC sensors have been widely used for sensing and actuating in SHM applications. PZT is relatively brittle and less flexible than MFC and PVDF. Despite the brittleness, PZT displays the highest stiffness and the highest transverse piezoelectric displacement coefficient (Shen 2009). The PZT sensor can generate much stronger excitations via elastic wave energies into the target structure when a harmonic voltage is applied on it. Therefore, PZT sensor was selected for the prototype design of the interface.

As shown in Fig. 6(b), the PZT interface is mounted on the surface of the host structure to monitor the changes in its structural properties which is induced by any structural damage. Under the high-frequency excitation $V(\omega)$ of the PZT sensor, the PZT interface interacts with the host structure via the coupling vibrations, as explained in the previous section. If the host structure is damaged, the coupling dynamic responses could be altered, making the variation of the EM impedance responses obtained from the interface.

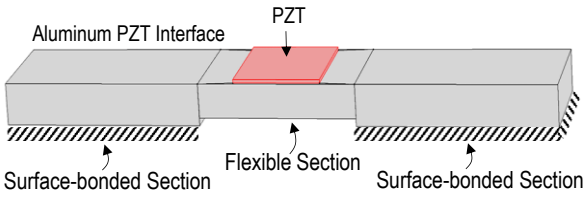

(a) Prototype of PZT interface

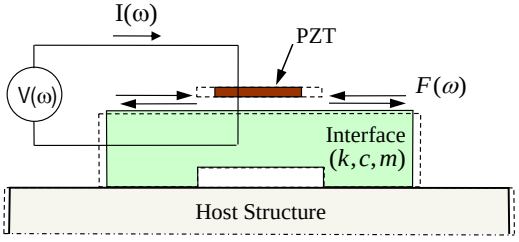

(b) PZT interface-host structure interaction

Fig. 6 Design of PZT interface device

3.2.2 Numerical impedance signatures of PZT interface

The effective frequency ranges of impedance signatures can be controlled by using the PZT interface for which its dynamic characteristics is closely associated with the resonant peaks of the impedance signatures. Therefore, it is needed to examine the local dynamic characteristics of the PZT interface. Based on the conceptual design of the PZT interface, a PZT interface example was selected, as shown in Fig. 7(a). Aluminum was selected for the interface's material. A PZT-5A patch sized 15x15 *mm* and thickness 0.51 *mm* was installed at the middle. The properties of the aluminium interface are specified as: Young's modulus E = 70.0 *GPa*, Poisson's ratio υ = 0.33, mass density ρ = 2700 kg/m^3, and damping loss factor η = 0.02. Also, the PZT patch was added by the piezoelectric material, PZT-5A, as listed in Table 2.

A FE model of the PZT interface was established by the commercial package, COMSOL Multi physics. The modules of Solid Mechanics and Piezoelectric Devices were used to perform the impedance analysis in the frequency domain. In FE modelling, the interface was discretized by 3D elastic solid elements FE and the fixed-fixed boundary condition as shown in Fig. 7(b). The meshing includes 608 solid elements (64 elements for the PZT patch and 544 elements for the interface body). To acquire the EM impedance responses, a harmonic excitation voltage with an amplitude of *1 V* was simulated to the top surface of the PZT patch element, and the bottom one was set as the ground electrode. Impedance responses of the PZT interface were numerically analysed, as shown in Fig. 8. The PZT interface shows the first and second peak frequencies at 19.18 *kHz* and 38.447 *kHz*, respectively.

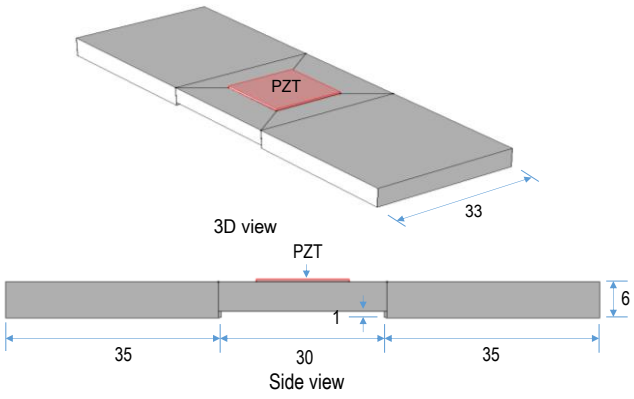

(a) Geometric sizes

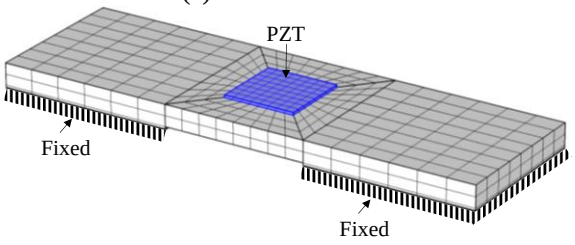

(b) Meshing and boundary conditions

Fig. 7 Geometries of PZT interface (mm)

Table 2 Properties of PZT-5A patch (eFunda Inc, 2010)

Parameters	Value
Elastic compliance, S_{ijkl}^{E} (m^2/N)	$\begin{pmatrix} 16.4 & -5.74 & -7.22 & 0 & 0 & 0 \\ -5.74 & 16.4 & -7.22 & 0 & 0 & 0 \\ -7.22 & -7.22 & 18.8 & 0 & 0 & 0 \\ 0 & 0 & 0 & 47.5 & 0 & 0 \\ 0 & 0 & 0 & 0 & 47.5 & 0 \\ 0 & 0 & 0 & 0 & 0 & 44.3 \end{pmatrix} \times 10^{-12}$
Dielectric coupling constant, d_{kij} (C/N)	$\begin{pmatrix} 0 & 0 & -171 \\ 0 & 0 & -171 \\ 0 & 0 & 374 \\ 0 & 584 & 0 \\ 584 & 0 & 0 \\ 0 & 0 & 0 \end{pmatrix} \times 10^{-12}$
Permittivity, ε_{jk}^{T} $(Farad/m)$	$\begin{pmatrix} 1730 & 0 & 0 \\ 0 & 1730 & 0 \\ 0 & 0 & 1700 \end{pmatrix} \times \left(8.854 \times 10^{-12}\right)$
Mass density, ρ (kg/m^3)	7750
Damping loss factor, η	0.005
Dielectric loss factor, δ	0.015

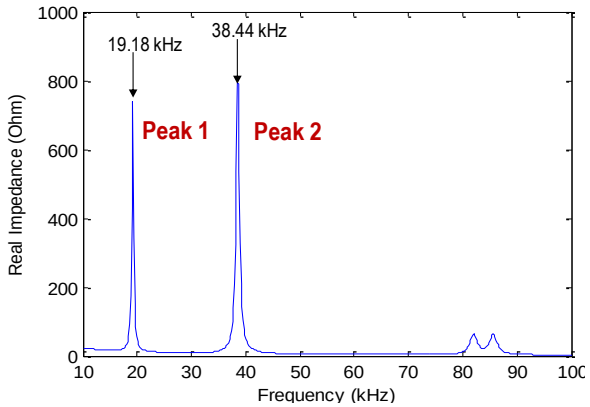

Fig. 8 Numerical impedance response of PZT interface

3.2.3 Modal analysis of PZT interface

The numerical modal analysis was performed for the PZT interface. The first four mode shapes representing the local vibration responses of the interface were obtained as shown in Fig. 9. Among them, Mode 1 is out-of-plane longitudinal flexural motion and Mode 4 is out-of-plane lateral flexural motion. Matching to the piezoelectric deformations of the PZT patch on the interface (as shown in Fig. 6), the longitudinal flexural motion (Mode 1) is identical to the first impedance peak (i.e., the first resonant frequency). Also, the longitudinal twist motion (Mode 4) is identical to the second impedance peak (i.e., the second resonant frequency).

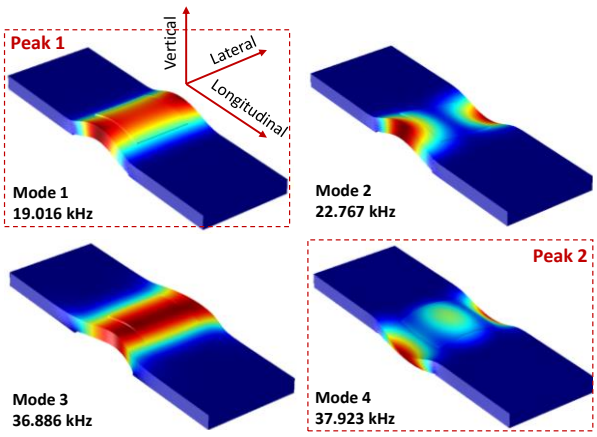

Fig. 9 Modal shapes of PZT interface corresponding to peak impedance responses (Huynh et al. 2015b)

From the comparison between Fig. 8 and Fig. 9, two modal shapes of the interface corresponding to the two resonant impedance peaks were numerically analysed as 19.016 *kHz* (Mode 1) and 37.923 *kHz* (Mode 4), respectively. It is observed that the first and second peaks of the impedance responses are identical to Modes 1 and 4 that represent the local vibration responses of the PZT interface.

3.2.4 Design rule of PZT interface

From the numerical analyses of Figs. 8 and 9, it is observed that the identified longitudinal and lateral flexural modes are corresponding to the resonant impedance peaks of the interface. It's worth noting that the frequency bands containing these impedance peaks are the effective frequency ranges. Therefore, the specifications of the interface device should be designed in such a way that its resonant frequencies f_n (of longitudinal and lateral flexural modes) can be within a predetermined effective frequency range $[f_s : f_e]$; in which f_s is the starting frequency and f_e is the ending frequency of a predefined range.

In practices, the design rule of the PZT interface can be made as follows: (1) the effective frequency range is predefined; (2) the material of the interface device is selected and the dimensions of the flexural section are determined using a criteria, $f_s < f_n < f_e$; and (3) the dimensions of the contact bodies are selected large enough to ensure the force and strain transfer through bonding layers.

3.3 Impedance monitoring of lab-scale tendon anchorage structure

As shown in Fig. 10(a), a lab-scaled tendon anchorage system was selected as the test structure. A 7-wire mono tendon (ϕ15.2 *mm*) was installed in length of 6.4 m by steel anchorage heads (ϕ45 *mm*) on bearing plates (100 *mm* × 100 *mm* × 10 *mm*) at two ends. Tension force was introduced into the cable by a stressing jack. A load cell was installed at one anchorage to measure the actual cable force.

The tendon was first pre-tensioned to T1 = 48.1 *kN* which was considered as the healthy state. For damage simulation, the tension force was reduced to T2 = 40.2 *kN*, T3 = 29.4 *kN* and T4 = 20.6 *kN*. For each damage case, five impedance measurements were conducted repeatedly. The room temperature was kept as close as constant of 23-24^oC by air conditioners during the tests.

The designed PZT interface was mounted on the surface of the bearing plate of the tendon-anchorage connection, as shown in Fig. 10(b). The PZT sensor was excited by a harmonic excitation voltage with 1*V*-amplitude, and the impedance signatures in 10-100 *kHz* were measured by a commercial impedance analyzer HIOKI 3532, see Fig. 10(c). As shown in Fig. 11, real impedance signatures were obtained in 10-100 *kHz* from the PZT interface. Two resonant frequencies were matching to the two frequency bands, 14-20 *kHz* (Peak 1) and 34-40 *kHz* (Peak 2). The tendon-force scenarios and the variation of the peak frequencies are outlined in Table 3. As the tendon force was gradually reduced from 48.1 *kN* (T1) to 20.6 *kN* (T4), the two peak frequencies were gradually decreased from 17.18 *kHz* to 16.68 *kHz* (Peak 1) and from 36.78 *kHz* to 35.60 *kHz* (Peak 2).

By relating the test results with the 2-DOF impedance model described previously, it is reasonable to conclude that the reduction in the peak frequencies (e.g., -2.91% in Peak 1 and -3.21% in Peak 2) indicates the reduction in the modal stiffness of the coupled interface-anchorage system. By noticing that the change in coupled impedance responses of the interface-anchorage was caused by the change in tendon forces, it is also reasonable to confirm the relationship between the tendon force and the stiffness of the interface-anchorage system. However, the decrement in peak frequencies was relatively small as compared with the decrement in tendon forces. The small variation of peak frequencies may cause difficulties when the PZT interface technique is implemented to realistic engineering structures under environmental and operational noises. For such real applications, data normalization methods based on cross-correlation, principal component analysis, and neural networks should be integrated with the PZT interface-based technique to eliminate the ambient noises (Koo *et al.* 2009, Lim *et al.* 2011, Huynh and Kim 2016).

The impedance signatures varied in magnitudes and peak frequencies as the tendon force was changed as observed from Fig. 11. In the impedance-based method, the damage assessment is conventionally made by the use of scalar damage indices, which allow easier quantification of the percentage of measured impedance signatures deviated from the baseline (Sun *et al.* 1995, Park *et al.* 2001, Park *et al.* 2003). To quantify the changes of impedance signatures, the RMSD (root-mean-square-deviation) index was employed as follows

$$RMSD(Z,Z^*)=\sqrt{\sum_{i=1}^{N}[Z^*(\omega_i)-Z(\omega_i)]^2\Big/\sum_{i=1}^{N}[Z(\omega_i)]^2} \quad (13)$$

where $Z(\omega_i)$ and $Z^*(\omega_i)$ are the impedance signatures measured at the i^{th} frequency before and after the prestress-loss event, respectively; and N denotes the number of frequency points in the sweep.

Fig. 12 shows RMSD indices calculated for the

impedance signatures of three frequency bands: 10-100 *kHz* (i.e., the whole frequency band), 10-20 *kHz* (i.e., the frequency band of Peak 1), and 30-40 *kHz* (i.e., the frequency band of Peak 2). The RMSD indices increased gradually as the tendon forces were reduced from T1 to T4. The RMSD indices of the second peak's frequency range (30-40 *kHz*) show a little more sensitive indication than that of the first peak's frequency range (10-20 *kHz*). As shown in Fig. 12, the RMSD variation between the tendon forces T2 and T3 was far less than the RMSD variation between T1 and T2 as well as the one between T3 and T4. This is because the variation of peak frequencies between the tendon forces T2 and T3 was less significant than those between T1 and T2 as well as T3 and T4, as observed in Table 3.

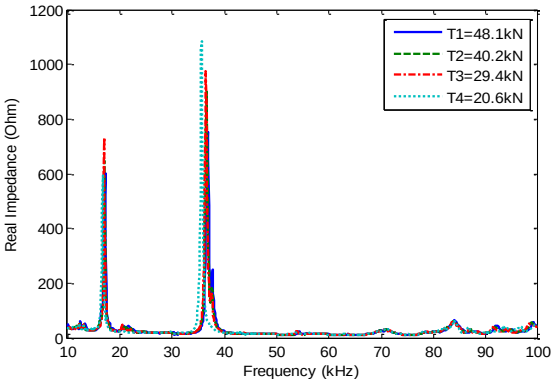

Fig. 11 Impedance signatures of the PZT interface under various tendon forces

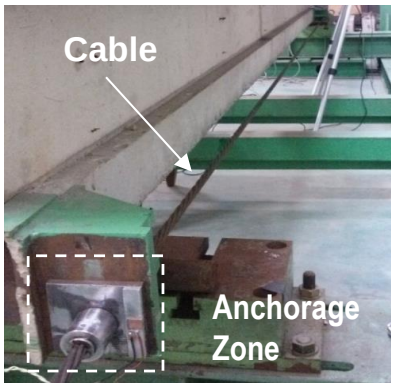

(a) Cable anchorage

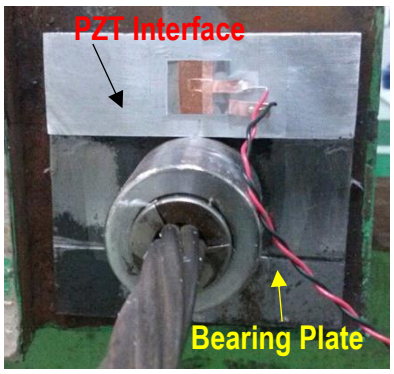

(b) Interface on bearing plate

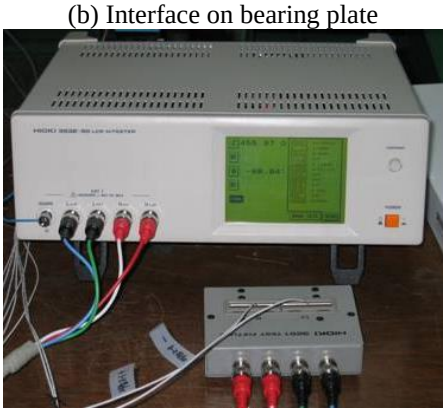

(c) Impedance analyzer HIOKI 3532

Fig. 10 Test setup for PZT interface-anchorage system

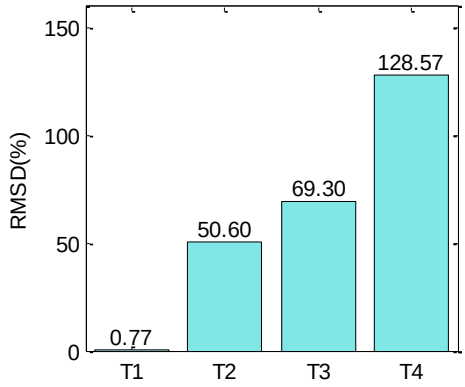

(a) 10-100 *kHz*

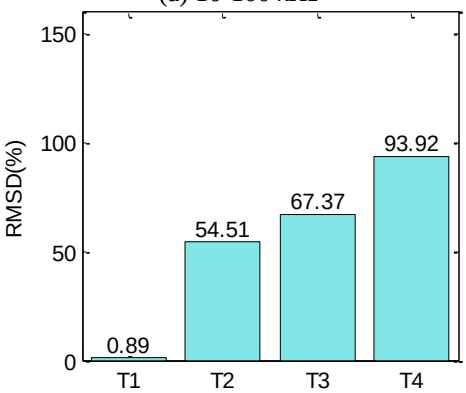

(b) 10-20 *kHz*

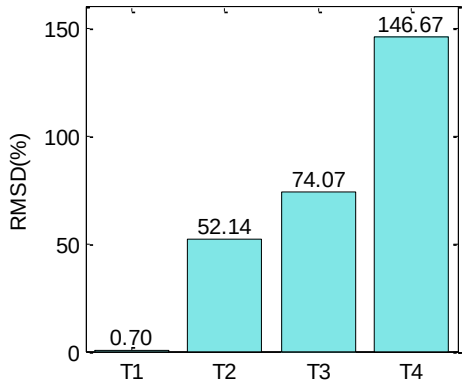

(c) 30-40 *kHz*

Fig. 12 Impedance monitoring results for four tendon-force levels

Table 3 Peak frequencies of PZT interface under various tendon-force levels

Case	Tendon Force Level (*kN*)	Peak 1		Peak 2	
		Frequency (*kHz*)	Variation (%)	Frequency (*kHz*)	Variation (%)
T1	48.1	17.18	0	36.78	0
T2	40.2	17.04	-0.81	36.62	-0.44
T3	29.4	17.00	-1.05	36.50	-0.76
T4	20.6	16.68	-2.91	35.60	-3.21

4. Quantitative damage identification of tendon anchorage

As described previously, impedance signatures were monitored for the various tendon forces of the test structure. The occurrence of damage (i.e., the change of tendon forces) could be alerted from the statistical classification of RMSDs. Thereafter, damage severities induced by the variation of tendon forces should be quantified to estimate the variation of structural performance with regards to its designed state. This goal is achieved by three steps: firstly, a FE model of the PZT interface-tendon anchorage system is simulated; secondly, a phase-by-phase model updating process is designed to fine-tune the FE model; finally, the model updating is performed to correlate the change in impedance signatures to the change in structural properties, both of which are induced by the variation of tendon forces.

4.1 Numerical modelling of tendon anchorage

As shown in Fig. 13, a FE model of the lab-scaled tendon anchorage with the PZT interface was established using COMSOL Multiphysics. The geometry of the FE model was in accordance with the real size of the target structure. As previously described in Fig. 5, the presence of the tendon force can be equivalently treated as the contact stiffness of the bearing plate. Then the loss of the tendon force can be simulated by the reduction of the contact stiffness. Hence, an equivalent contact spring system k_x, k_y and k_z was simulated for the test structure, as shown in Fig. 13. The loss factor of the contact damping is assumed as 0.02. The FE model was meshed by the 3D solids. A complete mesh consists of 1463 domain elements.

For simplification, the bonding layers between the PZT patch and the interface were not considered. The material properties of the aluminum interface were input to the FE model, as specified previously. The properties of the steel tendon anchorage were specified as: Young's modulus E = 200 *GPa*, Poisson's ratio υ = 0.3, mass density ρ = 7850 kg/m^3, and damping loss factor η = 0.02. The material properties of the PZT patch were input as listed in Table 2. The initial contact stiffness parameters were selected as: $k_x = k_y = 0$ and $k_z = 10^6$ $N/m/m^2$ (by assuming negligible x-y directional stiffness relative to z directional stiffness). The numerical modal analysis was performed for the PZT interface on the tendon anchorage, see Fig. 13(b). Note that the two mode shapes are corresponding to the two impedance peaks of the PZT interface on the tendon anchorage.

To acquire the electro-mechanical impedance, a harmonic voltage of 1V-amplitude was simulated to the top surface of the PZT patch, and the bottom one was set as the ground electrode. As shown in Fig. 14, real parts of impedance signatures were generated from the initial FE model. Two significant impedance peaks were identified at f_1 = 18.16 *kHz* (Peak 1) and f_2 = 36.96 *kHz* (Peak 2).

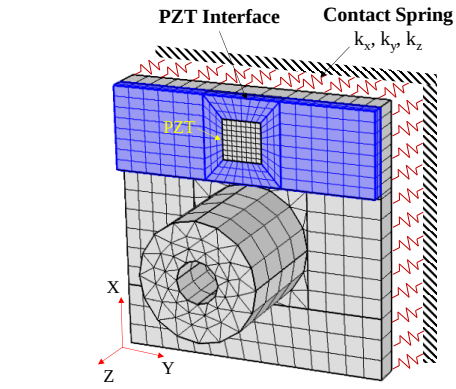

(a) FE model

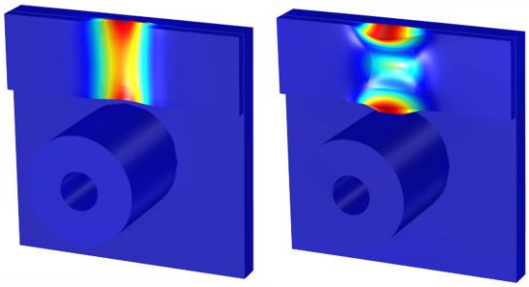

(b) Interface's two model responses

Fig. 13 FE model of tendon anchorage with PZT interface

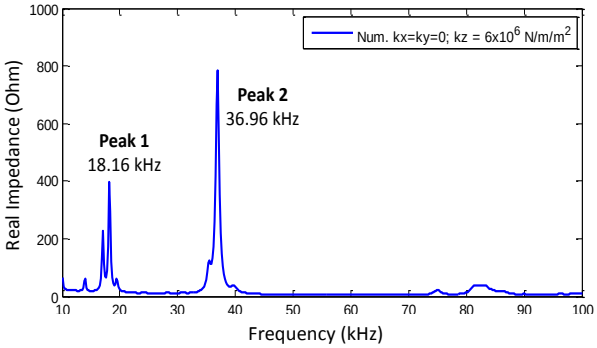

Fig. 14 Numerical impedance signatures of initial FE model of tendon-anchorage connection

As compared to the experimental results shown in Fig. 11, the two calculated impedance peaks were respectively identical to the two experimental ones, even though they are different in the peak frequencies and peak magnitudes. The motions of the two impedance peaks were also generated as shown in Fig. 13(b). It is observed that the motion of Peak 1 is the longitudinal flexural mode while that of Peak 2 is the lateral flexural mode.

4.2 Phase-by-phase model updating algorithm

The contact stiffness identification of the tendon anchorage is performed to quantitatively correlate the changes in the impedance signatures to the changes in structural properties and to identify the damage severity. A phase-by-phase model updating process is designed to fine-tune the contact stiffness of the FE model of the tendon anchorage. As described previously, the local dynamic responses of the interface device would be unchanged unless the structural parameters of the tendon anchorage and/or the interface device are altered. By assuming the interface itself remains undamaged, the local dynamic characteristics of the interface anchorage can be utilised as the indicator for the contact stiffness condition. That is, the contact stiffness of the lab-scaled tendon anchorage can be identified when the impedance peaks obtained from the corresponding FE model are well-matched with the experimental results.

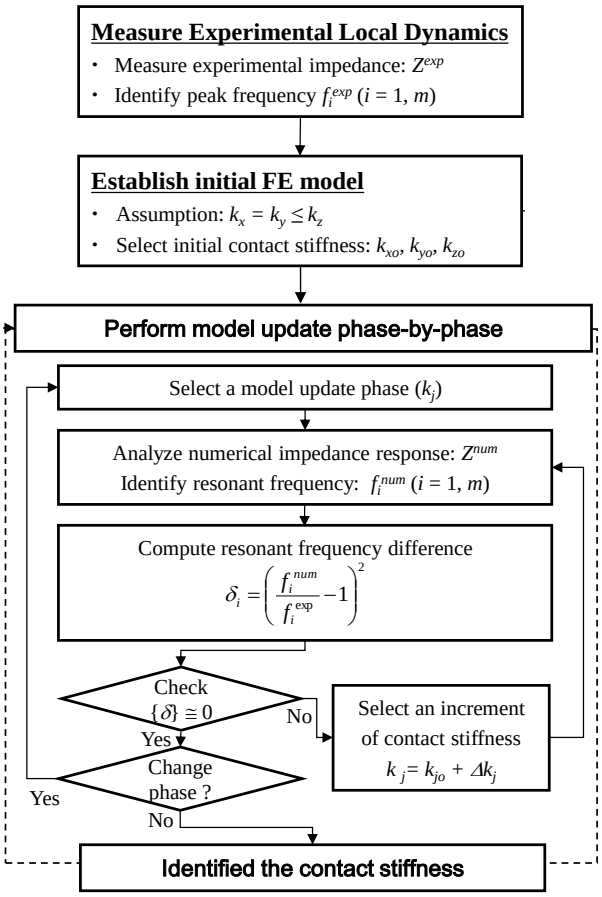

Fig. 15 Model updating algorithm for contact stiffness identification

The phase-by-phase model updating algorithm was designed as shown in Fig. 15. This algorithm is based on the sensitivity of the model updating parameters (Ho *et al.* 2012, Huynh *et al.* 2016b). The parameter having higher sensitivity to the structural change would be selected to be updated first. As reported by Ritdumrongkul *et al.* (2004), the variation of lateral contact stiffness (i.e., k_x and k_y) has relatively small effect as compared to that of axial contact stiffness (i.e., k_z). Therefore, the model update was performed for the phase k_z first, and next was the phase k_x. It should be noted that this model updating process needs to be performed in combination with the FE modelling at each iteration step.

The model updating process to identify the contact stiffness is outlined as follows:

(1) To experimentally measure impedance responses (e.g., peak frequencies) and to identify local dynamic characteristics (e.g. mode shapes and natural frequencies) of the interface;
(2) To establish an equivalent FE model of the target tendon anchorage and to select initial values of contact springs (k_x k_y and k_z);
(3) To perform model update phase for contact stiffness k_j (j = z, x) and to compute numerical impedance peaks;
(4) To check frequency errors between experimental and numerical impedance peaks and to decide an increment of the k_j contact stiffness; and
(5) To run Steps 3 and 4 repeatedly and to converge into ignorable errors.

4.3 Identified contact stiffness of tendon anchorage

The model updating process was carried out for the tendon anchorage using the impedance signatures measured from the PZT interface. The contact stiffness corresponding to the tendon force inflicted to the test structure was identified by minimizing the difference between the numerical impedance signatures of the FE model (e.g., Fig. 14) and the experimental results of identical patterns at the same frequency range (e.g., Fig. 11).

At first, the model updating was performed for the tendon force T1 = 48.1 *kN*. To match the numerical impedance peaks (i.e., Peak 1 and Peak 2) to the experimental results for T1 = 48.1 *kN*, three model updating phases were performed. Fig. 16 shows convergences of two peak frequencies of impedance signatures during model updating iterations for the tendon force T1 = 48.1 *kN*. Fig. 17 shows the two peak frequencies of the selected impedance signatures during the model updating iterations. Table 4 outlines updated model parameters corresponding to the two peak frequencies during the model updating iterations for T1 = 48.1 *kN*.

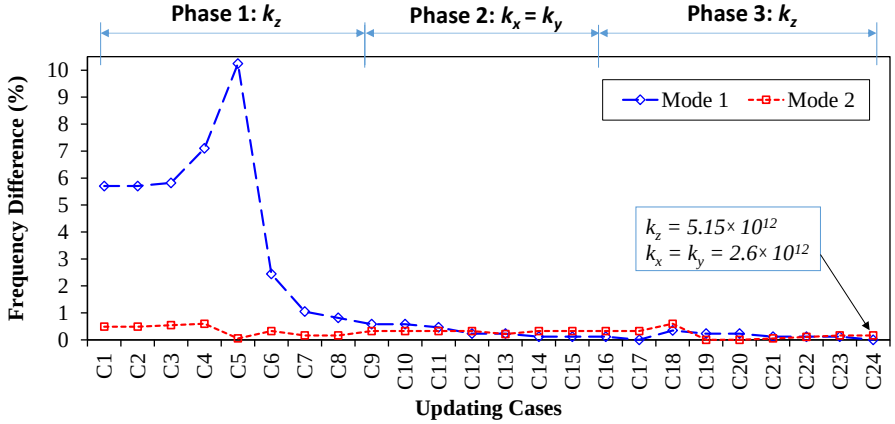

Fig. 16 Convergences of two peak frequencies of impedance signatures during model updating for T1 = 48.1 kN

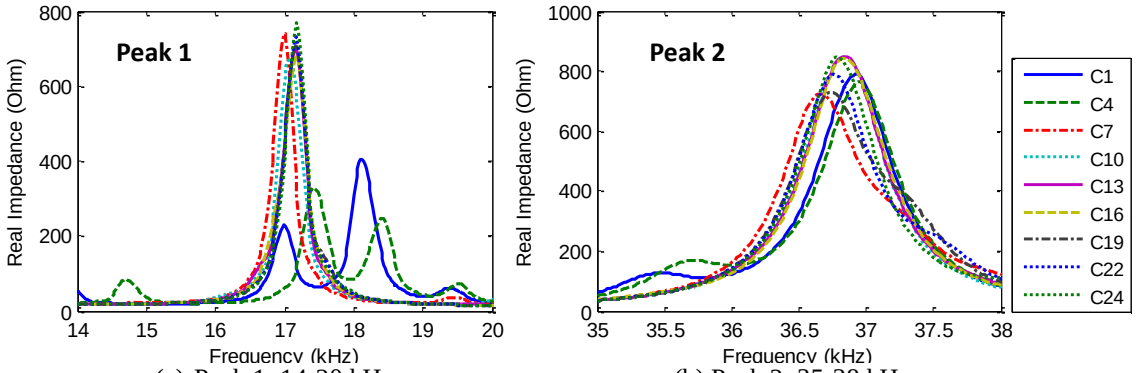

(a) Peak 1: 14-20 kHz (b) Peak 2: 35-38 kHz

Fig. 17 Two peak frequencies of impedance signatures during model updating for T1 = 48.1 kN

Table 4 Updated model parameters corresponding to two peak frequencies during model updating for T1 = 48.1 kN

Phase 1: Updating k_z									
Case	C1	C2	C3	C4	C5	C6	C7	C8	C9
Stiffness	1.0E+06	1.0E+08	1.0E+10	1.0E+11	1.0E+12	2.0E+12	3.0E+12	3.5E+12	4.0E+12
Peak 1	18.16	18.16	18.18	18.4	15.42	16.76	17	17.04	17.08
Peak 2	36.96	36.96	36.98	37.0	36.76	36.9	36.72	36.84	36.9
Phase 2: Updating k_x & k_y									
Case	C10	C11	C12	C13	C14	C15	C16		
Stiffness	1.0E+10	1.0E+11	1.0E+12	1.5E+12	2.0E+12	2.4E+12	2.6E+12		
Peak 1	17.08	17.1	17.14	17.14	17.16	17.16	17.16		
Peak 2	36.9	36.9	36.9	36.86	36.9	36.9	36.9		
Phase 3: Updating k_z									Target Frequency
Case	C17	C18	C19	C20	C21	C22	C23	C24	
Stiffness	4.2E+12	4.6E+12	4.7E+12	4.8E+12	4.9E+12	5.0E+12	5.1E+12	5.15E+12	
Peak 1	17.18	17.12	17.14	17.14	17.16	17.16	17.16	17.18	17.18
Peak 2	36.9	37.0	36.78	36.78	36.8	36.82	36.84	36.84	36.78

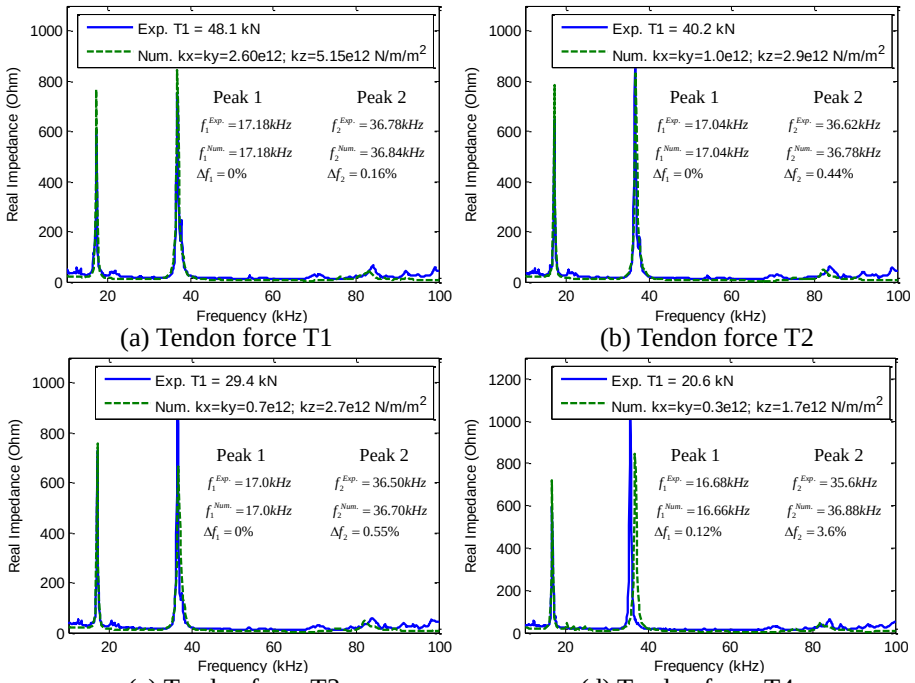

(a) Tendon force T1 (b) Tendon force T2

(c) Tendon force T3 (d) Tendon force T4

Fig. 18 Impedance signatures of updated FE models for four tendon forces T1-T4

In Phase 1, the updating phase for k_z was first performed. The contact stiffness k_z was gradually increased from the initial value $k_z = 10^6$ *N/m/m*^{2} to $k_z = 4\text{x}10^{12}$ *N/m/m*^{2} while the contact stiffness k_x and k_y remained as zero. After the first phase, the frequency errors converged from 5.7% to 0.58% for Peak 1 and 0.58% to 0.33% for Peak 2. Next, in Phase 2, the updating phase for k_x and k_y was performed.

The contact stiffness was gradually increased from the initial value $k_x = k_y = 0$ to $k_x = k_y = 2.6\text{x}10^{12}$ *N/m/m*^{2} while the contact stiffness k_z was remained unchanged. After the second phase, the frequency errors were reduced from 0.58 % to 0.12 % for Peak 1 and remained unchanged as 0.33 % for Peak 2. Finally, in Phase 3, the contact stiffness k_z was gradually increased from the initial value $k_z = 4\text{x}10^{12}$ *N/m/m*^{2} to $k_z = 5.15\text{x}10^{12}$ *N/m/m*^{2} while the contact stiffness k_x and k_y remained unchanged. After the third phase, the frequency errors converged from 0.58 % to 0 % for Peak 1 and 0.33 % to 0.16 % for Peak 2.

From the model updating iterations for T1 = 48.1 *kN*, it is observed that the two peak frequencies of the selected impedance signatures were changed in their magnitudes and frequencies during the model updating iterations (see Figs. 16 and 17). The frequency differences of Peak 1 and Peak 2 were decreased as the iteration C24 (see Fig. 16). The stiffness parameters were identified as the converged values when the peak frequencies of the updated FE model became identical to the experimental peak frequencies (see Table 4).

The same updating process was repeated for all tendon force cases T1-T4, from which the stiffness parameters corresponding to the four tendon forces were identified as shown in Fig. 18. In the figure, the numerical impedance signatures identified from the model updating processes were compared to the measured experimental ones (as shown in Fig. 11). It is observed that the numerical impedance responses were well-matched with the experimental results at the same frequency range and also identical patterns.

4.4 Quantitative identification of tendon anchorage damage

Relationships between the identified contact stiffness parameters (i.e., k_x, k_y and k_z) and the peak frequencies (i.e., Peak 1 and Peak 2) of impedance signatures were examined as shown in Fig. 19. Power functions were used to establish these relationships since they provided the good fits for the data. From using the relationships, the contact stiffness parameters of the tendon anchorage could be predicted for measured peak frequencies of impedance signatures. Note that the change in the contact stiffness causes the change in the peak frequencies. Note also that the peak frequencies represent the resonant responses of the PZT interface and the change in the impedance signatures is associated with the change in the dynamic properties of the structure. For the ignorable values of the contact stiffness such as the case C1 ($k_x = k_y = 0$ and $k_z = 10^6$ *N/m/m*^{2}), the peak height is small and position of the peaks is completely different from the other cases (as described in Fig. 17(a) and Ritdumronkul *et al.* (2004)). This means that the dynamic behaviours of the nearly-loosened tendon anchorage exhibit significantly different responses from the cases having relatively higher prestress forces. Hence, the relationships shown in Fig. 19 may not be applicable for estimating the contact stiffness for the completely unprestressed tendon anchorage.

As the final step, the relationship between the structural damage (i.e., prestress-loss events) and the structural properties (i.e., contact stiffness) is constructed for the quantitative damage severity estimation of the tendon-anchorage connection, as shown in Fig. 20. The relationships between the tendon forces and the contact stiffness k_x, k_y and k_z were fitted using the linear, quadratic, and exponential functions. By using the linear function, the correlation levels of fitted equations were computed as 0.8165 for k_x, k_y and 0.8376 for k_z while those of the

quadratic function were found as 0.8926 for k_x, k_y and 0.8601 for k_z. The correlation levels of the exponential function were calculated as 0.9532 for k_x, k_y and 0.8992 for k_z, as plotted in Fig. 20. Among the three fitting functions, the exponential functions provided the best fits for the data with higher correlation levels. From using the relationships shown in Fig. 20, the value of the prestress force could be predicted from the measured impedance signatures. It is observed that the severity of damage in the prestressed tendon anchorage can be quantitatively estimated by measuring impedance signatures and analysing equivalent structural parameters corresponding to the damaged state. It is also noted that the relationship between the identified contact stiffness and the prestress force may also be applicable for similar cable anchorage systems.

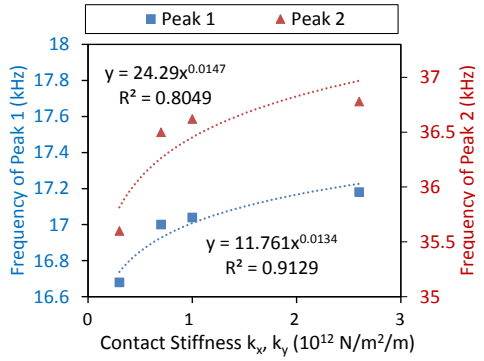

(a) Identified k_x and k_y

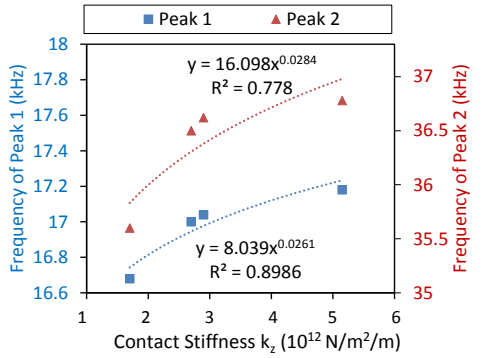

(b) Identified k_z

Fig. 19 Identified contact stiffness versus peak frequencies

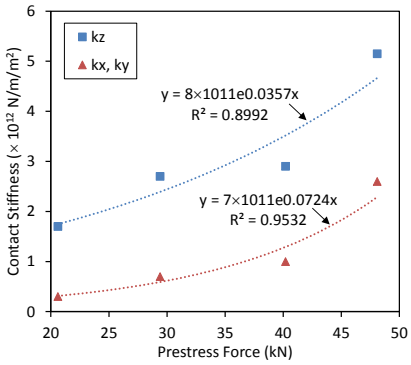

Fig. 20 Relationship between contact stiffness and prestress forces

5. Conclusions

In this study, the severity of damage in tendon anchorage caused by the loss of tendon forces was quantitatively identified by using the PZT interface-based impedance monitoring technique. Firstly, a 2-DOF impedance model was newly designed to represent coupled dynamic responses of PZT interface-host structure. Secondly, the 2-DOF impedance model was adopted for the tendon anchorage system. A prototype of PZT interface was designed for the impedance monitoring. Then impedance signatures were experimentally measured from a laboratory-scale tendon anchorage structure with various tendon forces. Finally, damage severities of the tendon anchorage induced by the variation of tendon forces were quantitatively identified from the phase-by-phase model updating process, from which the change in impedance signatures was correlated to the change in structural properties.

From the implementation of the 2-DOF impedance model, the relationship between the prestress force and the contact stiffness was identified for the tendon anchorage system. By using the relationship, the prestress force could be estimated from the measured impedance signatures. Thus, the damage severity of the prestressed tendon anchorage could be quantitatively estimated. From the findings, it is concluded that the proposed approach has the potential to quantitatively estimate the damage severity in the tendon anchorage which is caused by the tendon force-loss.

Acknowledgements

This work was supported by Basic Science Research Program of National Research Foundation of Korea (NRF) funded by the Ministry of Education (NRF 2016R1A2B4015087). The post-doctoral researcher involved in this research was also supported by the Brain Korea 21 Plus program of Korean Government.

References

Ayres, J.W., Lalande, F., Chaudhry, Z. and Rogers, C.A. (1998), "Qualitative impedance-based health monitoring of civil infrastructures", *Smart Mater. Struct.*, **7**(5), 599-605.

Bhalla, S. and Soh, C.K. (2004), "Electromechanical impedance modeling for adhesively bonded piezo-transducers", *J. Intel. Mat. Syst. Str.*, **15**(12), 955-972.

Chaudhry, Z., Lalande, F., Ganino, A., Rogers, C. and Chung, J. (1995), "Monitoring the integrity of composite patch structural repair via piezoelectric actuators/sensors", *Proceedings of the 36th Structures, Structural Dynamics and Materials Conference*, New Orleans, LA, USA.

COMSOL Inc., http://www.comsol.com

Doebling, S.W., Farrar, C.R. and Prime, M.B. (1998), "A summary review of vibration-based damage identification methods", *Shock Vib. Digest*, **30**(2), 91-105.

Efunda, Inc. (2010), http://www.efunda.com

Giurgiutiu, V. (2014), *Structural health monitoring with piezoelectric wafer active sensors*, 2nd Ed., Academic Press

Giurgiutiu, V. and Zagrai, A. (2005), "Damage detection in thin plates and aerospace structures with the electro-mechanical impedance method", *Struct. Health Monit.*, **4**(2), 99-118.

Ho, D.D., Kim, J.T., Stubbs, N. and Park, W.S. (2012), "Prestress-force estimation in PSC girder using modal parameters and system identification", *Adv. Struct. Eng.*, **16**(6), 997-1012.

Huynh, T.C. and Kim, J.T. (2014), "Impedance-based cable force monitoring in tendon-anchorage using portable PZT-interface technique", *Math. Probl. Eng.*, **2014**, 1-11.

Huynh, T.C. and Kim, J.T. (2016), "Compensation of temperature effect on impedance responses of PZT interface for prestress-loss monitoring in PSC girders", *Smart Struct. Syst.*, **17**(6), 881-901.

Huynh, T.C. and Kim, J.T. (2017), "FOS-Based prestress force monitoring and temperature effect estimation in unbonded tendons of PSC girders", *J. Aerospace Eng. - ASCE*, **30**(2), 1-14.

Huynh, T.C., Lee, K.S. and Kim, J.T. (2015b), "Local dynamic characteristics of PZT impedance interface on tendon-anchorage under prestress force variation", *Smart Struct. Syst.*, **15**(2), 375-393.

Huynh, T.C., Lee, S.Y., Kim, J.T., Park, W.S. and Han, S.H. (2013), "Simplified planar model for damage estimation of interlocked caisson system", *Smart Struct. Syst.*, **12**(3-4), 441-463.

Huynh, T.C., Nguyen, T.C., Choi, S.H. and Kim, J.T. (2016a), "Impedance monitoring at tendon-anchorage via mountable PZT interface and temperature-effect compensation", *Proceedings of SPIE*, **9799**, 1-6.

Huynh, T.C., Park, J.H. and Kim, J.T. (2016b), "Structural identification of cable-stayed bridge under back-to-back typhoons by wireless vibration monitoring", *Measurement*, **88**, 385-401.

Huynh, T.C., Park, Y.H., Park, J.H. and Kim, J.T. (2015a), "Feasibility verification of mountable PZT-interface for impedance monitoring in tendon-anchorage", *J. Shock Vib.*, **2015**, 1-11.

Johnson, K.L. (1985), *Contact mechanics*, Cambridge University Press, Cambridge.

Kim, J.T., Huynh, T.C. and Lee, S.Y. (2014), "Wireless structural health monitoring of stay cables under two consecutive typhoons", *Struct. Monit. Maint.*, **1**(1), 47-67.

Kim, J.T., Na, W.B., Park, J.H. and Hong, D.S. (2006), "Hybrid health monitoring of structural joints using modal parameters and EMI signatures", *Proceeding of SPIE*, San Diego, USA.

Kim, J.T., Park, J.H., Hong, D.S. and Park, W.S. (2010), "Hybrid health monitoring of prestressed concrete girder bridges by sequential vibration-impedance approaches", *Eng. Struct.*, **32**(1), 115-128.

Koh, Y.L., Chiu, W.K., Rajic, N. and Galea, S.C. (2003), "Detection of disbond growth in a cyclically loaded bonded composite repair patch using surface-mounted piezoceramic elements", *Struct. Health Monit.*, **2**(4), 327-339.

Koo, K.Y, Park, S.H., Lee, J.J. and Yun, C.B. (2009), "Automated impedance-based structural health monitoring incorporating effective frequency shift for compensating temperature effects", *J. Intel. Mat. Syst.Str.*, **20**(4), 367-377.

Li, H.N., Yi, T.H., Ren, L., Li, D.S. and Huo, L.S. (2014), "Review on innovations and applications in structural health monitoring for infrastructures", *Struct. Monit. Maint.*, **1**(1), 1-45.

Liang, C., Sun, F.P. and Rogers, C.A. (1994), "Coupled electro-mechanical analysis of adaptive material - Determination of the actuator power consumption and system energy transfer", *J. Intel. Mat. Syst. Str.*, **5**, 12-20.

Liang, C., Sun, F.P. and Rogers, C.A. (1996), "Electro-mechanical impedance modeling of active material systems", *Smart Mater. Struct.*, **5**(2), 171-186.

Lim, H.J., Kim, M.K., Sohn, H. and Park, C.Y. (2011), "Impedance-based damage detection under varying temperature and loading conditions", *NDT&E Int.*, **44**(8), 740–750.

Lopes, V., Park, G., Cudney, H.H. and Inman, D.J. (2000), "Impedance-based structural health monitoring with artificial neural networks", *J. Intel. Mat. Syst. Str.*, **11**(3), 206-214.

Min, J., Park, S. and Yun, C.B. (2010), "Impedance-based structural health monitoring using neural networks for autonomous frequency range selection", *Smart Mater. Struct.*, **19**(12), 1-10.

Min, J., Park, S., Yun, C.B., Lee, C.G. and Lee, G. (2012), "Impedance-based structural health monitoring incorporating neural network technique for identification of damage type and severity', *Eng. Struct.*, **39**, 210-220.

Nguyen, K.D. and Kim, J.T. (2012), "Smart PZT-interface for wireless impedance-based prestress-loss monitoring in tendon-anchorage connection", *Smart Struct. Syst.*, **9**(6), 489-504.

Ni, Y.Q., Ye, X.W. and Ko, J.M. (2010), "Monitoring-based fatigue reliability assessment of steel bridges: analytical model and application", *J. Struct. Eng. - ASCE*, **136**(12), 1563-1573.

Ni, Y.Q., Ye, X.W. and Ko, J.M. (2012), "Modeling of stress spectrum using long-term monitoring data and finite mixture distributions", *J. Eng. Mech. - ASCE*, **138(**2), 175-183.

Park, G., Cudney, H.H. and Inman, D.J. (2001), "Feasibility of using impedance-based damage assessment for pipeline structures", *Earthq. Eng. Struct. D.*, **30**(10), 1463-1474.

Park, G., Farrar, C.R., Rutherford, A.C. and Robertson, A.N. (2006), "Piezoelectric active sensor self-diagnostics using electrical admittance measurements", *J. Vib. Acoust.*, **128**(4), 469-476.

Park, G., Sohn, H., Farrar, C. and Inman, D. (2003), "Overview of piezoelectric impedance-based health monitoring and path forward", *Shock Vib. Digest*, **35**(6), 451-463.

Park, J.H., Huynh, T.C. and Kim, J.T. (2015), "Temperature effect on wireless impedance monitoring in tendon anchorage of prestressed concrete girder", *Smart Struct. Syst.*, **15**(4), 1159-1175.

Park, S., Park, G., Yun, C.B. and Farrar, C.R. (2009), "Sensor self-diagnosis using a modified impedance model for active sensing-based structural health monitoring", *Struct. Health Monit.*, **8**(1), 71-82.

Park, S., Yun, C.B., Roh, Y. and Lee, J. (2005), "Health monitoring of steel structures using impedance of thickness modes at PZT patches", *Smart Struct. Syst.*, **1**(4), 339-353.

Ritdumrongkul, S., Abe, M., Fujino, Y. and Miyashita, T. (2004), "Quantitative health monitoring of bolted joints using a piezoceramic actuator-sensor", *Smart Mater. Struct.*, **13**(1), 20-29.

Shen, D. (2009), "Piezoelectric energy harvesting devices for low frequency vibration applications", Ph.D. Thesis, Department of Materials Engineering, Auburn University, Alabama.

Soh, C.K., Tseng, K.K., Bhalla, S. and Gupta, A. (2000), "Performance of smart piezoceramic patches in health monitoring of a RC bridge", *Smart Mater. Struct.*, **9**(4), 533-542.

Stubbs, N. and Osegueda, R. (1990), "Global non-destructive damage evaluation in solids", *Int. J. Anal. Exp. Modal Anal.*, **5**(2), 67-79.

Sun, F.P., Chaudhry Z., Liang, C. and Rogers, C.A. (1995), "Truss structure integrity identification using PZT sensor-actuator", *J. Intel. Mat. Syst. Str.*, **6**(1), 134-139.

Xu, Y.G. and Liu, G.R. (2002), "A modified electro-mechanical impedance model of piezoelectric actuator-sensors for debonding detection of composite patches", *J. Intel. Mat. Syst. Str.*, **13**(6), 389-396.

Zagrai, A.N. and Giurgiutiu, V. (2001), "Electro-mechanical impedance method for crack detection in thin plates", *J. Intel.*

Mat. Syst. Str., **12**(10), 709-718.